Supplementary Information for:

Preferred Orientations of Organic Cations at Lead-Halide Perovskite Interfaces Revealed by Vibrational Sum-Frequency Spectroscopy

Woongmo Sung,[1,2] Christian Müller,[3,4] Sebastian Hietzschold,[3,4] Robert Lovrinčić,[3,4] Nathaniel P. Gallop,[5] Artem A. Bakulin,[5] Satoshi Nihonyanagi,[1,2] Tahei Tahara[1,2]

[1] Molecular Spectroscopy Laboratory, RIKEN, 2-1 Hirosawa, Wako, Saitama 351-0198, Japan

[2] Riken Center for Advanced Photonics, RIKEN, 2-1 Hirosawa, Wako, Saitama 351-0198, Japan

[3] InnovationLab GmbH, Speyerer Str. 4, 69115 Heidelberg, Germany

[4] Institute for High-Frequency Technology, TU Braunschweig, Schleinitzstrasse 22, 38106, Braunschweig, Germany

[5] Department of Chemistry, Imperial College London, Molecular Sciences Research Hub, 80 Wood Lane, London, W12 0BZ, United Kingdom

Keywords: Lead Halide Perovskite; Hole Transport Layer; Methylammonium Cation; Interface; Nonlinear Optical Spectroscopy

Contents:

S1. Sample morphology characterisation

Film thicknesses and morphologies were determined using Scanning Electron Microscopy (SEM). A focused ion beam was used to create cross sections of $MAPbX_3$ and $FAPbX_3$ on several substrates, which were then subsequently imaged using SEM. For each sample, several film thickness values were obtained at a variety of locations along the cross section with the film thicknesses estimated as an average of these values. Estimates of the thickness of the Spiro-MeOTAD and PCBM layers could not be obtained for these samples, although earlier studies have obtained thicknesses of 150—250 nm and 60—100 nm for Spiro-MeOTAD and PCBM respectively. An example FIB cross-section is displayed in Fig. S1. SEM micrographs, illustrating the morphologies of each sample are given in Fig. S2.

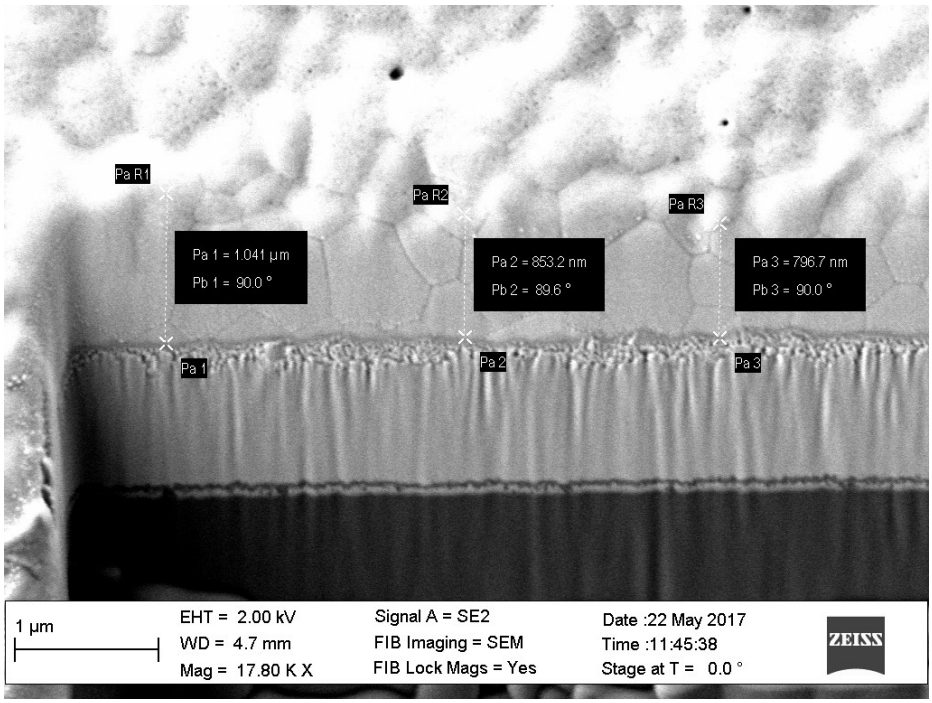

Fig. S1: SEM cross-section of $MAPbBr_3$ deposited on NiO.

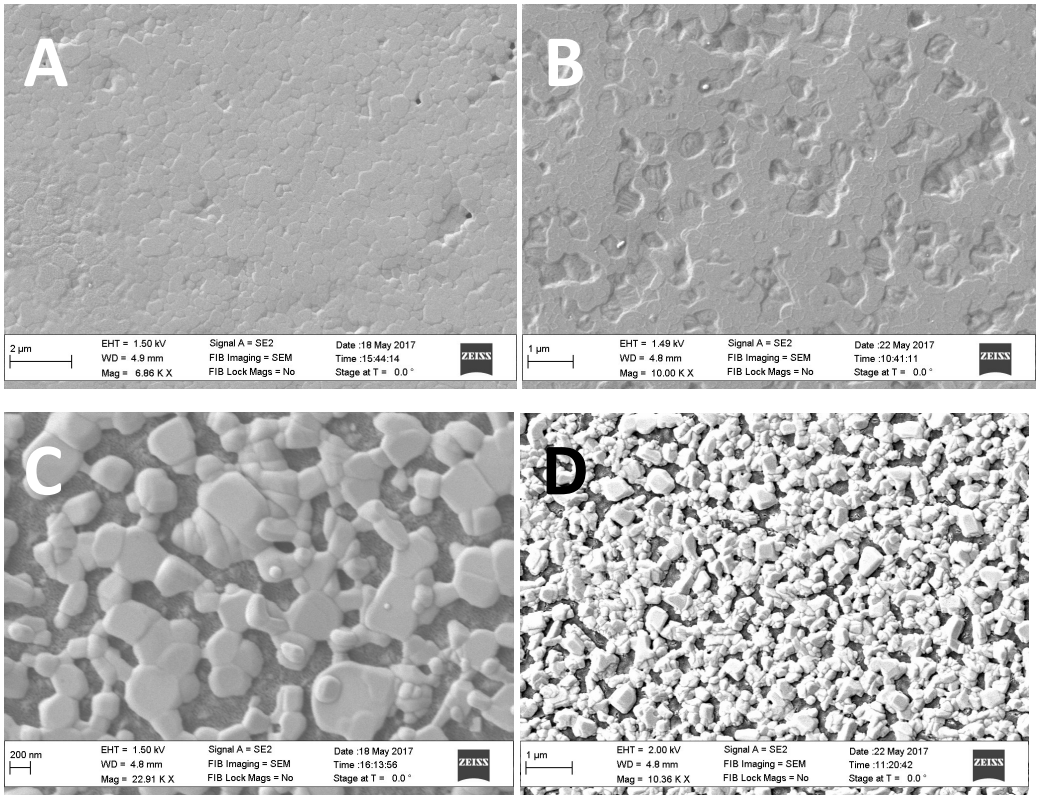

Fig S2: SEM micrographs of (A) $MAPbBr_3$ on TiO_2; (B) $MAPbBr_3$ on NiO_x; (C) $CsPbBr_3$ on TiO_2; (D) $CsPbBr_3$ on NiO_x.

S2. Sample IR charecterisation

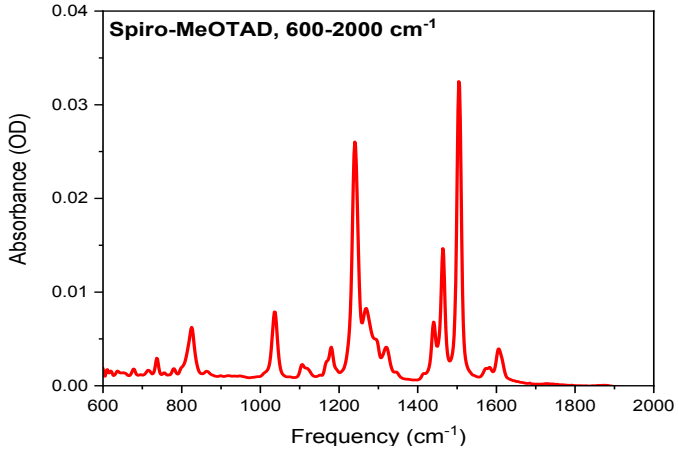

Fig. S3: IR spectrum of Spiro-MeOTAD, including the IR fingerprint region.

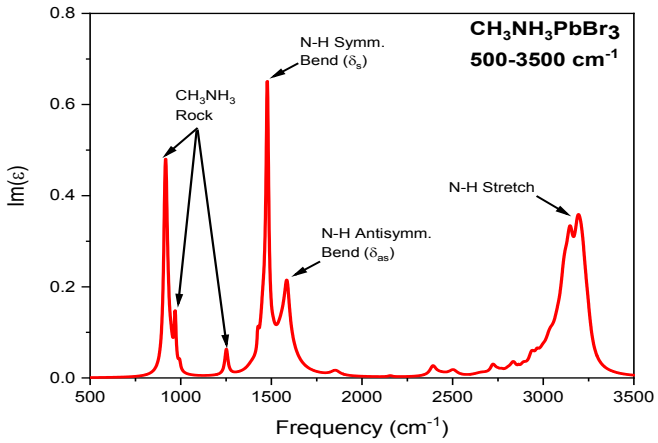

Fig S4: Calculated imaginary components of the dielectric constant of, $MAPbBr_3$. Key spectral assignments are provided. Data taken from Ref. 1.

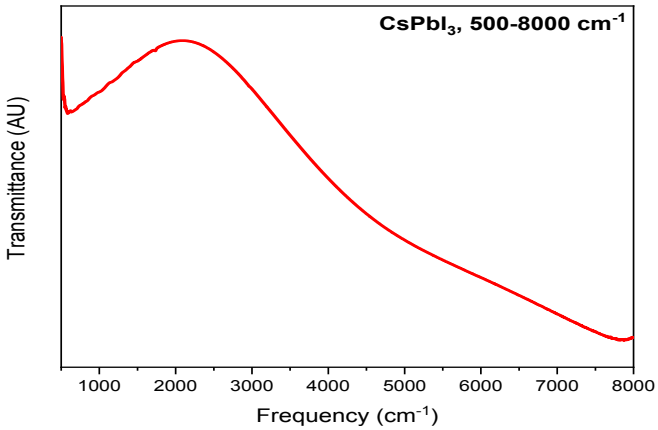

Fig. S5: IR Spectrum of $CsPbI_3$ demonstrating the absence of discrete vibrational peaks.

S3. Calculation on Fresnel factors

For PPP polarization combination, effective second-order susceptibility, $\chi^{(2)}_{eff,\,PPP}$ is a linear combination of second-order susceptibility tensor components, $\chi^{(2)}_{ijk}$ in which dummy indices i, j, and k are either x or z in our laboratory coordinates as described in Fig. S6(a). For a single interface having azimuthal isotropy and showing no multiple reflection, explicit version of eq. 1 in the main text is given as[2],

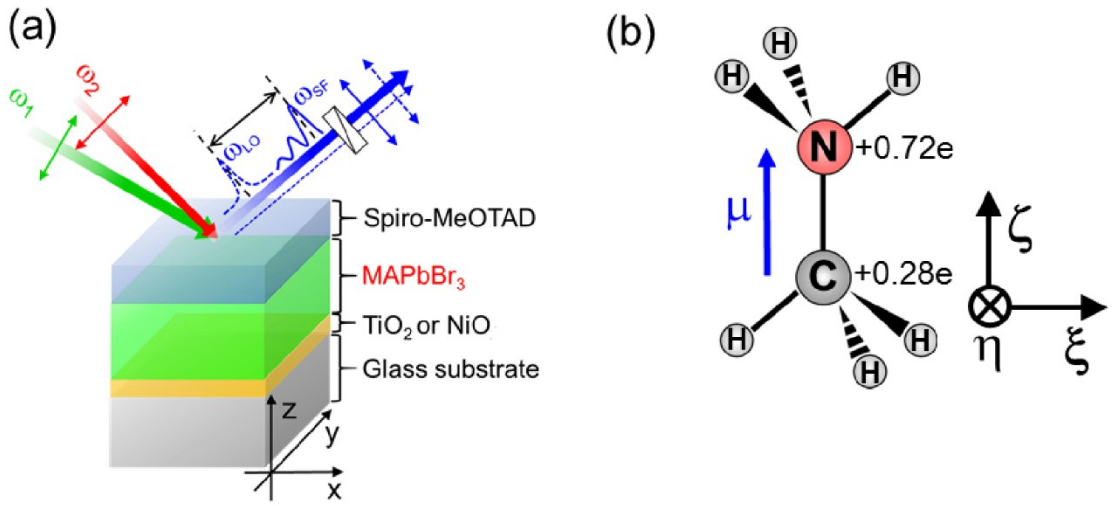

Figure S6. Beam geometry and laboratory coordinates for HD-VSFG experiment on the perovskite multilayer sample. (b) Picture of MA cation showing Mulliken charges with hydrogens summed into heavy atoms and molecular coordinates.

$$\chi^{(2)}_{eff,PPP} = -L_{xx}(\omega_3)L_{xx}(\omega_1)L_{zz}(\omega_2)\cos\beta_3\cos\beta_1\sin\beta_2\chi^{(2)}_{xxz}$$
$$-L_{xx}(\omega_3)L_{zz}(\omega_1)L_{xx}(\omega_2)\cos\beta_3\sin\beta_1\cos\beta_2\chi^{(2)}_{xzx}$$
$$+L_{zz}(\omega_3)L_{xx}(\omega_1)L_{xx}(\omega_2)\sin\beta_3\cos\beta_1\cos\beta_2\chi^{(2)}_{zxx}$$
$$+L_{zz}(\omega_3)L_{zz}(\omega_1)L_{zz}(\omega_2)\sin\beta_3\sin\beta_1\sin\beta_2\chi^{(2)}_{zzz}$$
$$\sim -L_{xx}(\omega_3)L_{xx}(\omega_1)L_{zz}(\omega_2)\cos\beta_3\cos\beta_1\sin\beta_2\chi^{(2)}_{xxz}$$
$$+L_{zz}(\omega_3)L_{zz}(\omega_1)L_{zz}(\omega_2)\sin\beta_3\sin\beta_1\sin\beta_2\chi^{(2)}_{zzz}$$
$$= -C_{xxz}\chi^{(2)}_{xxz} + C_{zzz}\chi^{(2)}_{zzz} \quad \cdots(S1)$$

where the subscripts 1, 2, and 3 stand for incident visible, IR, and emitted SF, respectively, and $L_{ii}(\omega_m)$ is a Fresnel factor of laboratory coordinate (I = x, z) for ω_m beam (m = 1, 2, 3), and β_m is angle of incident/emission for ω_m beam. In this expression, Fresnel factors $L_{xx}(\omega_m)$ and $L_{zz}(\omega_m)$ are given by[2],

$$L_{xx}(\omega_m) = \frac{2n_1(\omega_m)\cos\gamma_m}{n_1(\omega_m)\cos\gamma_m + n_2(\omega_m)\cos\beta_m}$$
$$L_{zz}(\omega_m) = \frac{2n_2(\omega_m)\cos\beta_m}{n_1(\omega_m)\cos\gamma_m + n_2(\omega_m)\cos\beta_m}\left(\frac{n_1(\omega_m)}{n'(\omega_m)}\right)^2 \cdots(S2)$$

where n_1 and n_2 are the refractive indices for two mediums forming the interface, and n' is the refractive index of the interface lies between n_1 and n_2, and γ_m is the refraction angle of beam having an incidence angle of β_m in the medium 1. In this analysis, we took n' as an average value between n_1 and n_2. The coefficients C_{xxz} and C_{zzz} are product among the Fresnel factors, thus positive. As discussed in the following section, multiple reflection effect gives additional phase rotation on the Fresnel factors.

In our experiment, incident angles of ω_1 and ω_2 are ~50° and ~40°, respectively. Then, refraction angle at air/Spiro-MeOTAD interface is ~27° for ω_1, and ~26° for ω_3. At the second interface of Spiro-MeOTAD/$MAPbBr_3$, the refraction angles are ~23° for ω_1, and ~22° for ω_3. For ω_2, refraction angle either for air/Spiro-MeOTAD and Spiro-MeOTAD/$MAPbBr_3$ depends on frequency since there exists large dispersion in refractive index of Spiro-MeOTAD as shown in Fig. S6(b). Therefore, C_{xxz} and C_{zzz} in eq. 1 in the main text are functions of ω_2 frequency. Since extinction coefficient κ of Spiro-MeOTAD and $MAPbBr_3$ at the probing IR region are not negligible, we use complex refractive indices for Fresnel factor calculation. In cases of ω_1 and ω_3, the refractive indices of Spiro-MeOTAD and $MAPbBr_3$ are almost real, and dispersion is small. So, we set $n(\omega_1) \sim n(\omega_3) = 1.96$ for $MAPbBr_3$ and $n(\omega_1) \sim n(\omega_3) = 1.70$ for Spiro-MeOTAD[3].

We now consider multiple reflections of beams occurring each side of Spiro-MeOTAD film. For simplicity, we calculated modified Fresnel factors for three-layer system consisting of air, Spiro-MeOTAD, and $MAPbBr_3$, and neglect contribution from other layers underneath. According to the previous investigations of VSFG spectroscopy on three-layer system, equations for effective second-order susceptibility in eq. S1 can be modified as below,

$$\begin{aligned}\chi^{(2)}_{eff,PPP} \sim & -L^{\mathrm{I}}_{xx}(\omega_3)L^{\mathrm{I}}_{xx}(\omega_1)L^{\mathrm{I}}_{zz}(\omega_2)\cos\beta_3\cos\beta_1\sin\beta_2\chi^{(2),\mathrm{I}}_{xxz} \\ & + L^{\mathrm{I}}_{zz}(\omega_3)L^{\mathrm{I}}_{zz}(\omega_1)L^{\mathrm{I}}_{zz}(\omega_2)\sin\beta_3\sin\beta_1\sin\beta_2\chi^{(2),\mathrm{I}}_{zzz} \\ & - L^{\mathrm{II}}_{xx}(\omega_3)L^{\mathrm{II}}_{xx}(\omega_1)L^{\mathrm{II}}_{zz}(\omega_2)\cos\beta_3\cos\beta_1\sin\beta_2\chi^{(2),\mathrm{II}}_{xxz} \\ & + L^{\mathrm{II}}_{zz}(\omega_3)L^{\mathrm{II}}_{zz}(\omega_1)L^{\mathrm{II}}_{zz}(\omega_2)\sin\beta_3\sin\beta_1\sin\beta_2\chi^{(2),\mathrm{II}}_{zzz} \quad \cdots(\mathrm{S3})\end{aligned}$$

where the first and the second terms represent SF response from the first interface (air/ Spiro-MeOTAD: Ⅰ) and the remaining two terms correspond to SF from the second interface (Spiro-MeOTAD/$MAPbBr_3$: Ⅱ). From HD-VSFG measurement on Spiro-MeOTAD film deposited on glass substrate, we found that the SF signal from the air/Spiro-MeOTAD interface is negligibly small

comparing to that from Spiro-MeOTAD/$MAPbBr_3$ interface. Therefore, we can neglect first two terms in equation S3. Modified Fresnel factors at Spiro-MeOTAD/$MAPbBr_3$ interface which include multiple reflections are described as follows[4, 5],

$$L_{xx}^{\mathrm{II}}(\omega_m) = \exp(i\Delta_2(\omega_m))\frac{t_{p,12}(\omega_m)(1-r_{p,23}(\omega_m))}{1+r_{p,12}(\omega_m)r_{p,23}(\omega_m)\exp(i\Delta_1(\omega_m))}\frac{\cos\beta_m'}{\cos\beta_m}$$

$$L_{zz}^{\mathrm{II}}(\omega_m) = \exp(i\Delta_2(\omega_m))\frac{t_{p,12}(\omega_m)(1+r_{p,23}(\omega_m))}{1+r_{p,12}(\omega_m)r_{p,23}(\omega_m)\exp(i\Delta_1(\omega_m))}\frac{n_1(\omega_m)n_2(\omega_m)}{(n_{2,3}'(\omega_m))^2}\cdots(\mathrm{S4})$$

where n_1, n_2, n_3 are complex refractive indices for medium 1 (air), 2 (Spiro-MeOTAD), and 3 ($MAPbBr_3$), and $n_{2,3}'$ is refractive index of Spiro-MeOTAD/$MAPbBr_3$ interface. $t_{p,jk}$ and $r_{p,jk}$ are transmission and reflection coefficients at interface of medium j and k. β_m and β_m' correspond to incident angle of the ω_m beam at the first and second interface, respectively. Δ_1 corresponds to change in phase of SF signal caused by multiple reflection. An equation for Δ_1 is given by,

$$\Delta_1(\omega_m) = \frac{2\omega_m}{c}n_2(\omega_m)d\cos\beta_m'\cdots(\mathrm{S5})$$

where d is ~200 nm for the Spiro-MeOTAD layer. Δ_2 stands for relative phase difference between two SF signals generated from two different interfaces. As the air/Spiro-MeOTAD interface gives almost no SF response, Δ_2 can be assumed to be zero. Then, eq. S3 is further simplified as below[4, 5],

$$\begin{aligned}\chi_{eff,PPP}^{(2)} &\sim -L_{xx}^{\mathrm{II}}(\omega_3)L_{xx}^{\mathrm{II}}(\omega_1)L_{zz}^{\mathrm{II}}(\omega_2)\cos\beta_3\cos\beta_1\sin\beta_2\chi_{xxz}^{(2),\mathrm{II}}\\ &+L_{zz}^{\mathrm{II}}(\omega_3)L_{zz}^{\mathrm{II}}(\omega_1)L_{zz}^{\mathrm{II}}(\omega_2)\sin\beta_3\sin\beta_1\sin\beta_2\chi_{zzz}^{(2),\mathrm{II}}\\ &= -C_{xxz}^{\mathrm{II}}\chi_{xxz}^{(2),\mathrm{II}} + C_{zzz}^{\mathrm{II}}\chi_{zzz}^{(2),\mathrm{II}}\quad\cdots(\mathrm{S6})\end{aligned}$$

For simplicity we omitted superscript II in the equations of the main text. Using the refractive indices shown in Fig. S7, the values of C^{II}_{xxz} and C^{II}_{zzz} are calculated and these values are shown in Fig. S8. In Fig. S8(a) and S8(b), the values between 1509 and 1517 cm^{-1} are missing since refractive index of the Spiro-MeOTAD film goes below 1, and the ω_2 beam at air/Spiro-MeOTAD interface shows total external reflection. Phase of the coefficient C^{II}_{xxz} and C^{II}_{zzz} is ~4° for the frequency corresponding to

δ_{as} mode and ~6° to ~27° for the δ_s mode region as shown in Fig. S8(b). Thus, the real parts of the coefficients are almost same as the amplitude in Fig. S8(a), and the C_{xxz} and C_{zzz} in the main text have positive sign for the ω_2 frequencies of δ_s mode and δ_{as} mode. We used the amplitudes of the coefficients at 1480 and 1580 cm^{-1} for calculating $\chi^{(2)}_{eff,\ PPP}$ of δ_s and δ_{as} modes, respectively. For ammonium moiety having C_{3v} symmetry, $\chi_{xxz}^{(2),\,II}$ and $\chi_{zzz}^{(2),\,II}$ are given as[4,5],

$$\chi_{xxz}^{(2),II} = \frac{1}{2}N_S[-\beta_{\zeta\xi\xi}^{(2)}(\langle\cos\theta\rangle - \langle\cos^3\theta\rangle) + \beta_{\zeta\zeta\zeta}^{(2)}((1+r)\langle\cos\theta\rangle - (1-r)\langle\cos^3\theta\rangle)]$$
$$\chi_{zzz}^{(2),II} = N_S[\beta_{\zeta\xi\xi}^{(2)}(\langle\cos\theta\rangle - \langle\cos^3\theta\rangle) + \beta_{\zeta\zeta\zeta}^{(2)}(r\langle\cos\theta\rangle + (1-r)\langle\cos^3\theta\rangle)]$$
$$r = \beta_{\xi\xi\zeta}^{(2)} / \beta_{\zeta\zeta\zeta}^{(2)} \cdots (S7)$$

where *N*s is surface number density of ammonium moiety, $\beta_{\zeta\zeta\zeta}^{(2)}$ and $\beta_{\zeta\xi\xi}^{(2)}$ are second-order hyper-polarizability tensor components, θ is polar angle between C-N dipole of methyl ammonium ion and the surface normal (z-axis) of the perovskite film as described in Fig. S6. The brackets mean average over orientational distribution of ammonium moieties in the detection area of the HD-VSFG measurement. As shown in the section S4, $\beta_{\zeta\zeta\zeta}^{(2)}$ and $\beta_{\zeta\xi\xi}^{(2)}$ are mainly contributed to δs and δas modes, respectively. So, at each of resonance conditions, $\chi_{xxz}^{(2),\,II}$ and $\chi_{zzz}^{(2),\,II}$ are approximated to,

$$\text{For } \omega_2 = \omega_{\delta s},\ \chi_{xxz}^{(2),II} \sim \frac{1}{2}N_S\beta_{\zeta\zeta\zeta}^{(2)}((1+r)\langle\cos\theta\rangle - (1-r)\langle\cos^3\theta\rangle)$$
$$\chi_{zzz}^{(2),II} \sim N_S\beta_{\zeta\zeta\zeta}^{(2)}(r\langle\cos\theta\rangle + (1-r)\langle\cos^3\theta\rangle) \cdots (S8)$$

$$\text{For } \omega_2 = \omega_{\delta as},\ \chi_{xxz}^{(2),II} \sim -\frac{1}{2}N_S\beta_{\zeta\xi\xi}^{(2)}(\langle\cos\theta\rangle - \langle\cos^3\theta\rangle)$$
$$\chi_{zzz}^{(2),II} \sim N_S\beta_{\zeta\xi\xi}^{(2)}(\langle\cos\theta\rangle - \langle\cos^3\theta\rangle) \cdots (S9)$$

By substituting eq. S8 and S9 into eq. S6, the effective second-order susceptibility is given as,

$$\chi_{eff,PPP}^{(2)} \sim -\frac{1}{2}C_{xxz}^{II}N_S\beta_{\zeta\zeta\zeta}^{(2)}((1+r)\langle\cos\theta\rangle - (1-r)\langle\cos^3\theta\rangle)$$
$$+C_{zzz}^{II}N_S\beta_{\zeta\zeta\zeta}^{(2)}(r\langle\cos\theta\rangle + (1-r)\langle\cos^3\theta\rangle),\ \text{at } \omega_2 = \omega_{\delta s} \cdots (S10)$$

$$\chi_{eff,PPP}^{(2)} \sim \frac{1}{2}C_{xxz}^{II}N_S\beta_{\zeta\xi\xi}^{(2)}(\langle\cos\theta\rangle - \langle\cos^3\theta\rangle)$$
$$+C_{zzz}^{II}N_S\beta_{\zeta\xi\xi}^{(2)}(\langle\cos\theta\rangle - \langle\cos^3\theta\rangle),\ \text{at } \omega_2 = \omega_{\delta as} \cdots (S11)$$

Eqs. S10 and S11 correspond to Eqs. 2 and 3 in the main text.

In addition, we checked that multiple reflection between the two interfaces of Spiro-MeOTAD/$MAPbBr_3$ and $MAPbBr_3/TiO_2$ gives only small modulation in phase of the Fresnel factors. For the ω_1 visible probe beam (λ~795 nm) and the ω_3 SF signal (λ~706 nm) at the resonance of δ_{as} mode, corresponding refractive index of TiO_2 is ~2.52 and ~2.55, respectively[6]. Therefore, refractive index difference between $MAPbBr_3$ (n~1.96) and TiO_2 is ~0.6, and reflection coefficient r_p is ~0.11 at $MAPbBr_3/TiO_2$ interface. On the other hand, refractive index of $MAPbBr_3$ at IR frequency (ω_2) of 1580 cm^{-1} (n~2.15) is well-matched with TiO_2 refractive index (~2.06)[7], and reflection coefficient is close to zero. Considering three-layer thin film system consisting of Spiro-MeOTAD, $MAPbBr_3$, and TiO_2, the modified Fresnel factors for Spiro-MeOTAD/$MAPbBr_3$ interface are, $L_{xx}(\omega_1)$ = 1.05-0.01i, $L_{xx}(\omega_2)$ = 0.79, $L_{xx}(\omega_2)$ = 0.97-0.1i, $L_{zz}(\omega_1)$ = 0.82+0.01i, $L_{zz}(\omega_2)$ = 0.78, and $L_{zz}(\omega_3)$ = 0.87+0.09i. From these values, coefficients for $\chi^{(2)}_{xxz}$ and $\chi^{(2)}_{zzz}$ are 0.29-0.03i and 0.05+0.005i, respectively. The corresponding phase change is about 6°.

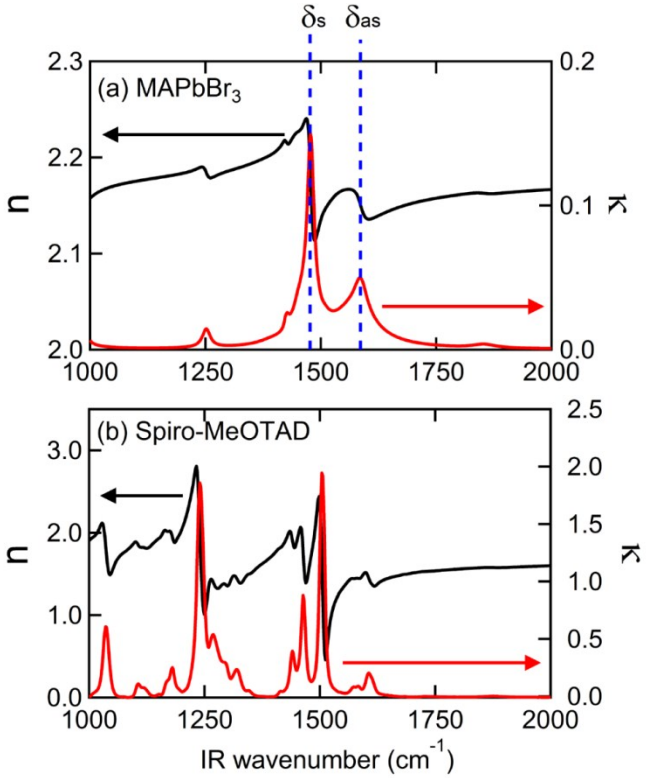

Figure S7. Complex refractive indices (Red: *n* and black: *k*) of (a) $MAPbBr_3$ calculated from complex dielectric constant listed in Ref. 1 and (b) Spiro-MeOTAD obtain from an IR absorption spectrum of 20 nm Spiro-MeOTAD film.

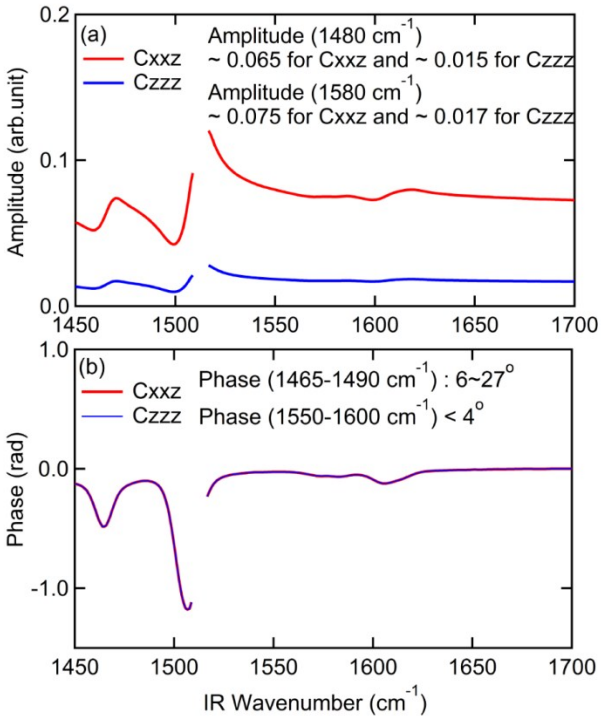

Figure S8. (a) Amplitude and (b) phase of complex coefficients Cxxz and Czzz including multiple reflection effect.

S4. DFT calculation and second-order hyperpolarizability

From DFT calculation (Gaussian09, B3LYP/6-311++G(d,p)) of a methylammonium cation in vaccumm, we obtained polarizability and dipole derivatives for calculating second-order hyperpolarizaiblity tensor components. Table S1 and S2 show lists of dipole and polarizability derivatives for ammonium bending modes.

Table S1. Dipole derivatives for δ_s and δ_{as} modes

Frequency (cm^{-1})	Mode	$\partial\mu/\partial\xi$ (a.u.)	$\partial\mu/\partial\eta$ (a.u.)	$\partial\mu/\partial\zeta$ (a.u.)
1536	δ_s	0.02	0.00	-1.04x10[1]
1671	δ_{as}	-6.42	0.02	0.00
1671	δ_{as} (degenerated)	0.00	6.41	0.00

Table S2(a). Polarizability derivative tensor components (a. u.) for δ_s mode

Coordinate	ξ	η	ζ
ξ	0.73×10^{-1}	0.00	0.00
η	0.00	0.71×10^{-1}	0.00
ζ	0.00	0.00	-0.49

Table S2(b). Polarizability derivative tensor components (a. u.) for δ_{as} mode

Coordinate	ξ	η	ζ
ξ	0.31	0.00	-0.49
η	0.00	-0.31	0.00
ζ	-0.49	0.00	0.94x10-3

Table S2(c). Polarizability derivative tensor components (a. u.) for δ_{as} (degenerate) mode

Coordinate	ξ	η	ζ
ξ	0.00	0.31	0.00
η	0.31	0.00	0.49
ζ	0.00	0.49	0.00

Then, second-order hyperpolarizability tensor component is proportional to product between dipole and polarizability derivatives[8]. The calculated tensor components for δ_s mode are $\beta^{(2)}_{\xi\xi\zeta} = -0.76$, $\beta^{(2)}_{\zeta\zeta\zeta} = 5.10$, $\beta^{(2)}_{\xi\,\zeta\,\xi} = 0$, $\beta^{(2)}_{\zeta\,\xi\,\xi} = 0$ and for δ_{as} mode $\beta^{(2)}_{\xi\xi\zeta} = 0$, $\beta^{(2)}_{\zeta\zeta\zeta} = 0$, $\beta^{(2)}_{\xi\,\zeta\,\xi} = 3.15$, $\beta^{(2)}_{\zeta\xi\xi} = 3.15$.

S5. XRD Analysis

To confirm the phase purity of samples produced using our synthesis method, we performed X-ray Diffraction (XRD) on a set of films produced under an identical procedure to those subjected to HD-vSFG spectroscopy. XRD analysis was performed using a benchtop diffractometer (D2 Phaser, Bruker Inc.). The diffraction pattern was scanned in the range 2θ = 10—50° with a resolution of 0.05°, using the Cu-K_α line (1.5406 Å) as the X-ray source. Fig. S8 displays the obtained XRD pattern. Comparison of the obtained XRD pattern with standard patterns for the cubic and orthorhombic phases, obtained from the Inorganic Crystal Structure Database (ICSD # 29073 and ICSD # 97851, respectively) is provided in Fig. S9. Our obtained XRD pattern matches well with the standard pattern for the cubic phase. We also note that the peak splitting at 2θ≈30°, characteristic of the orthorhombic phase of $CsPbBr_3$, is absent. On this basis, we conclude that the dominant phase in our samples is the cubic phase.

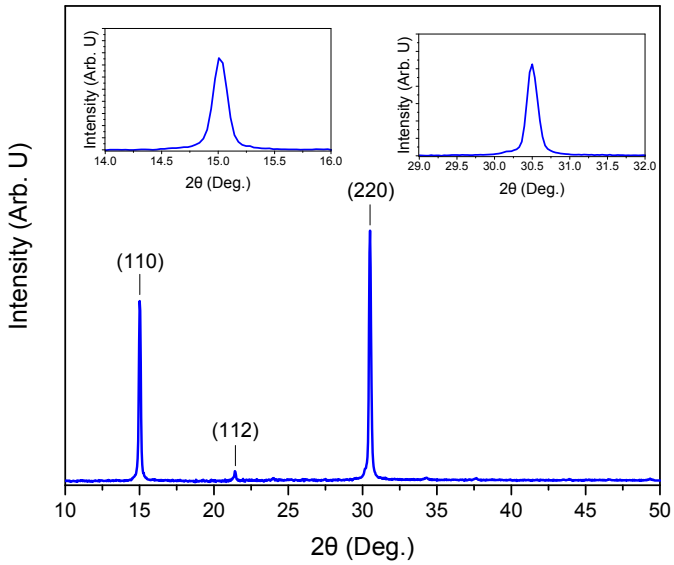

Fig. S8: Representative XRD pattern for the as-synthesised $CsPbBr_3$ films.

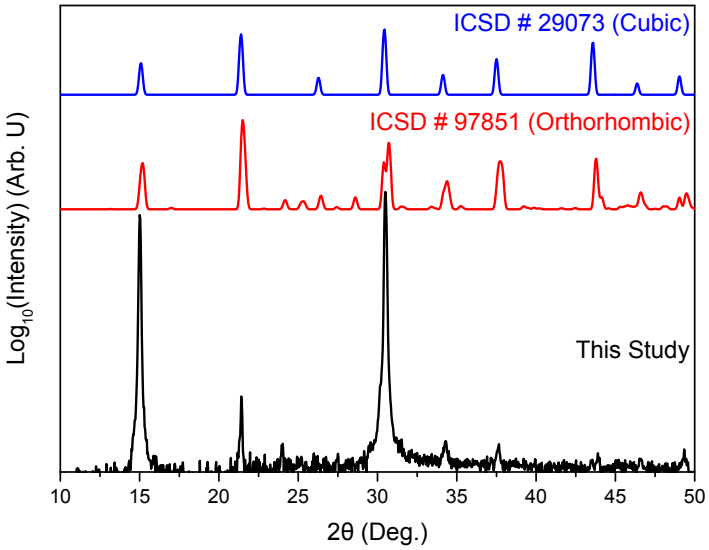

Fig. S9: Comparison of XRD pattern displayed in Fig. S8 with standard patterns for the orthorhombic and cubic phases of $CsPbBr_3$, obtained from the Inorganic crystal structure database.

References

(1) Glaser, T.; Müller, C.; Sendner, M.; Krekeler, C.; Semonin, O. E.; Hull, T. D.; Yaffe, O.; Owen, J. S.; Kowalsky, W.; Pucci, A.; et al. Infrared Spectroscopic Study of Vibrational Modes in Methylammonium Lead Halide Perovskites. *J. Phys. Chem. Lett.* **2015**, *6*, 2913–2918.

(2) Zhuang, X.; Miranda, P.; Kim, D.; Shen, Y., Mapping molecular orientation and conformation at interfaces by surface nonlinear optics. *Phys. Rev. B* **1999**, *59*, 12632.

(3) Brittman, S.; Garnett, E. C. Measuring n and k at the Microscale in Single Crystals of $CH_3NH_3PbBr_3$ Perovskite. *J. Phys. Chem. C* **2015**, *120*, 616-620.

(4) Tong, Y.; Zhao, Y.; Li, N.; Osawa, M.; Davies, P. B.; Ye, S., Interference effects in the sum frequency generation spectra of thin organic films. I. Theoretical modeling and simulation. *J. Chem. Phys.* **2010**, *133*, 034704.

(5) Backus, E. H.; Garcia-Araez, N.; Bonn, M.; Bakker, H. J., On the role of Fresnel factors in sum-frequency generation spectroscopy of metal–water and metal-oxide–water interfaces. *J. Phys. Chem. C* **2012**, *116*, 23351-23361.

(6) DeVore, J. R.; Refractive indices of rutile and sphalerite *J. Opt. Soc. Am.* **1951**, *41*, 416-419.

(7) Kischkat, J.; et al. Mid-infrared optical properties of thin films of aluminum oxide, titanium dioxide, silicon dioxide, aluminum nitride, and silicon nitride. *Appl. opt.* **2012**, *51*, 6789-6798.

(8) Ishiyama, T.; Imamura, T.; Morita, A. Theoretical studies of structures and vibrational sum frequency generation spectra at aqueous interfaces. *Chem. Rev.* **2014**, *114*, 8447-8470.